JOURNAL OF GEOPHYSICAL RESEARCH, VOL. 106, NO. A12, PAGES 29,645–29,653, DECEMBER 1, 2001

Microscopic signatures of the bipartite auroral oval: FAST measurements

W. J. Peria and M. J. Brittnacher

Department of Earth and Space Sciences, University of Washington, Seattle, Washington, USA

G. K. Parks and C. W. Carlson

Space Sciences Laboratory, University of California, Berkeley, California, USA

Abstract. The separation of the nightside auroral oval into two distinct regions, sometimes referred to as a "double oval," is often observed during substorm recovery in global images from the Ultraviolet Imager (UVI) experiment. The two regions of auroral emission are both extended for a few hours of magnetic local time and are separated from one another by a few degrees in magnetic latitude. High-resolution, low-altitude data from the FAST spacecraft reveal that the two regions (1) represent distinct types of electron precipitation, (2) contain distinct types of ion distributions, and (3) are accompanied by a regular and repeatable field-aligned current pattern. A region of corotating plasma is often observed in conjunction with the equatorward region. The low-altitude particle measurements indicate that the equatorward emission is caused by the diffusion into the loss cone of ~2 keV electrons from the plasma sheet, while the poleward emission is caused by the electrostatic acceleration of electrons at much lower altitudes. The two regions represent electron energy fluxes of roughly the same magnitude (although the poleward flux is larger), but the poleward flux carries a substantial field-aligned current, while the equatorward flux does not. This low-altitude current pattern, interpreted in terms of ionospheric stress applied by convective flow in the tail, indicates that the equatorward emission is associated with very weak and uniform high-altitude flow, while the poleward emission is at the footpoint of strongly sheared duskward flow.

1. Bipartite Auroral Oval

The auroral oval is often observed to be divided into two distinct parts. More precisely, there are two concentric partial rings of auroral emission (called herein the equatorward and poleward ovals), which are extended for several hours in magnetic local time and separated by a few degrees of magnetic latitude. This two-part structure is relatively steady and exists on timescales long compared to any auroral activity (i.e., brightening and fading) which may be present. The detailed time development of the bipartite oval, and its relation to substorms, has been presented previously by *Elphinstone et al.* [1995a, 1995b]. They assert that there are two source regions for discrete auroral arcs and that postexpansion phase activity in the midnight sector of the poleward oval is consistent with reconnection occurring in the distant tail ($-X_{\mathrm{GSE}} \geq 30\ R_E$). *Sanchez et al.* [1993], again in the context of substorm dynamics, discuss a "flux depletion region," which almost certainly corresponds to the gap between the two parts of the bipartite oval.

Paper number 2000JA000357.
0148-0227/01/2000JA000357$09.00

In this paper, we ask, what microphysical processes are operating to produce UV emission in the two separate regions of the bipartite oval? We proceed by examining, in detail, data from the overflight of a typical nightside bipartite oval by the FAST spacecraft. These microscopic data reveal that distinctly different physical processes are operating to produce emission in each of the two regions. Emission in the equatorward oval is produced by hot, unaccelerated electron precipitation, characteristic of the plasma sheet. A structured ion signature is seen throughout the equatorward oval, with generally larger ion energies being observed at higher latitudes. At the poleward edge of the equatorward oval, the structured ions abruptly disappear. The poleward emission is produced by intense, electrostatically accelerated "inverted V" precipitation. These electrons have a degree of field alignment which is greatest when their characteristic energy is changing most rapidly. Ion precipitation in the poleward oval is very weak, with no distinctive energy or angular features.

The detailed event analysis which we present in this paper is consistent with the well-known overall tendency of aurorae toward discreteness at the poleward boundary of the auroral oval. Our main purpose is to show, in detail, using the best data currently available, the microscopic physics as-

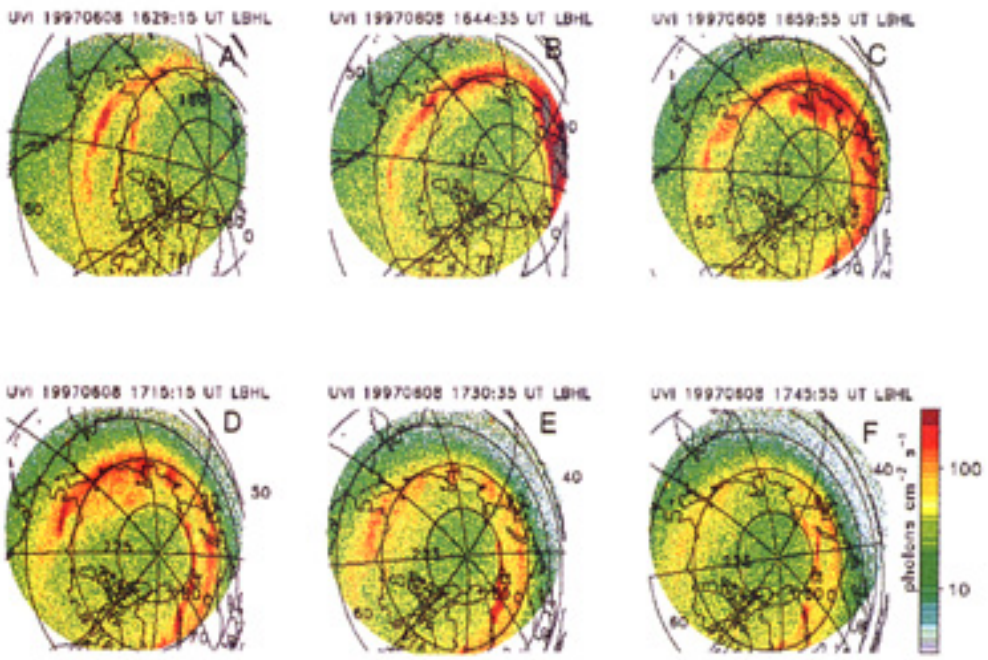

Plate 1. An overview of a typical bipartite auroral event. The FAST overflight occurred between the recording of Plates 1d and 1e.

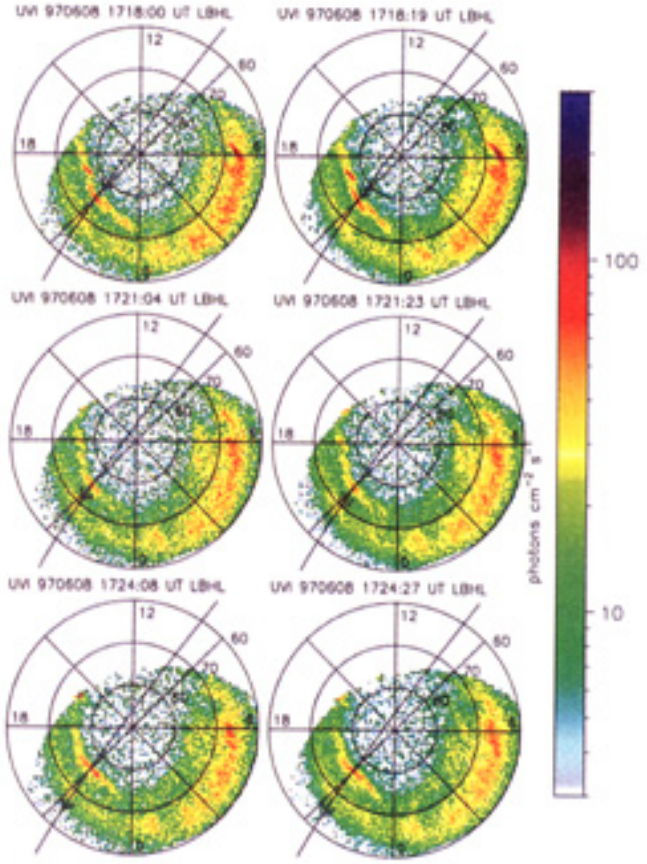

Plate 2. Images of the bipartite oval during the FAST overflight. The location of FAST and its direction of travel, at the beginning and end of each exposure, are indicated by the double arrowhead. A star-derived pointing correction was used to produce this plate.

sociated with this commonly observed auroral morphology: the bipartite oval. In addition, we show that the brightness of UV emissions from the aurora is not necessarily a measure of the current carried on the corresponding flux tubes, that significant UV emission can come from unaccelerated electron precipitation, and that corotating plasma can exist on flux tubes which map to the plasma sheet.

2. Methodology

We coordinate the data from three different instrument suites in this study. First, we use the global images from the Ultraviolet Imager (UVI) to identify bipartite oval events, to observe their time evolution, and to provide a context for the microscopic data. Ground-based magnetometer data are used to determine the temporal context of each bipartite oval event. Finally, the FAST data are used to examine and differentiate among various physical processes at work in the bipartite oval and derive information about the global convection and current pattern. The event we chose to examine, while typical in many respects, is unusual in that the entire nightside auroral zone is in sunlight. There are therefore plentiful atmospheric photoelectrons throughout. We will make use of these electrons to infer the presence or absence of significant acceleration potential on each part of the pass.

UVI measures ultraviolet emission in the Lyman-Birge-Hopfield (LBH) wavelengths in two bands: LBHs (140-160 nm) and LBHl (160-180 nm). The auroral emissions measured through the LBHl filter are expected to be proportional to the total energy flux deposited into the ionosphere by electrons over the 1-10 keV energy range. This critical result is arrived at through computationally intensive modeling of the transport processes of auroral electrons [*Lummerzheim et al.*, 1997]. The LBHs data share this proportionality to energy flux but are also inversely proportional to the characteristic energy of the precipitating electrons. This is because energetic electrons penetrate more deeply into the neutral atmosphere before producing emission, and such emission is then partially absorbed as it propagates back upward. The LBHl and LBHs images will show the same intensities for precipitation with a characteristic energy of roughly 5 keV, while a harder precipitation spectrum will produce a dimmer LBHs image. For a more detailed description of the UVI instrument, see *Torr et al.* [1995].

There is, at times, a substantial discrepancy between the electron energy flux measured by FAST and that inferred from UVI images, with UVI indicating a larger energy flux. It is possible that for at least some of these times, the additional LBH emission (beyond that expected from the measured precipitating electron energy flux) is produced by precipitating ions. The effectiveness of ions at producing LBH emissions remains controversial at the time of this writing. We have been unable to show a systematic relation between the UVI-FAST discrepancy and the precipitating ion energy flux. Furthermore, for the event shown in this paper the integrated (over energy and pitch angle) ion energy flux is always smaller than the corresponding electron energy flux. The maximum integrated ion energy flux in this event is <0.2 erg cm^{-2} s^{-1}. Therefore we do not believe that ions played a significant role in producing the LBH emissions shown in this paper.

The effective spatial resolution of UVI is 40 x 400 km, which is clearly not sufficient to resolve individual discrete arcs. UVI usually acquires an image in 18 or 37 s, during which time the FAST spacecraft will have moved at least 90 or 180 km. The great strength of UVI is the global context it provides for all other auroral measurements. In this study the UVI data were used to identify events which had a reasonably steady bipartite oval structure occurring in the premidnight sector.

The FAST satellite carries instruments for measuring both ion and electron distribution functions and electric and magnetic fields. FAST makes measurements in the auroral zone at altitudes between 300 and 4300 km. The FAST electrostatic analyzers (ESAs) provide continuous coverage of all pitch angles, at a time resolution of at least 80 ms (corresponding to spatial structures of 500 m or less), for electrons and ions with energies per unit charge from roughly 5 eV to 30 keV. The ESAs include a deflection system, which insures that the geomagnetic field remains within their field of view under most operating conditions. We use the FAST electron and ion data to infer conditions on flux tubes sampled by FAST in crossing the equatorward and poleward ovals and to compute the precipitating energy flux, net fluxes, effective temperatures, and characteristic energies. For a complete description of the FAST instrumentation, see *Carlson et al.* [1998].

FAST magnetometer data are used in this study to determine the strength and polarity of field-aligned currents, or, alternatively, the degree of shear in the magnetospheric flow. The interpretation of magnetic perturbations as the signature of magnetospheric flow is not entirely straightforward. Besides the usual space-time ambiguity, there is always uncertainty as to whether a particular magnetic field gradient is due to sheared flow in the outer magnetosphere or due to ionospheric conductivity gradients. In addition, some magnetic perturbations are due to Alfven waves, which propagate along flux tubes as the magnetosphere and ionosphere come to equilibrium following a disturbance; that is, they are not the signature of steady flow. On the other hand, intervals where the magnetic perturbations vanish are unambiguous; no stress is applied to the ionosphere in such regions, and certainly no current is flowing there. Also, even when the high- and low-altitude flows are decoupled (e.g., by a parallel electric field), the magnetic perturbations can indicate the direction of the high-altitude flow.

The electric field instrument on FAST yields information about the plasma flow local to the spacecraft. However, since the DC electric field is measured only in the spacecraft spin plane (which is roughly the same as its orbit plane), only the component of flow normal to the spin plane (roughly perpendicular to the spacecraft velocity) can be deduced.

We utilize ground-based magnetometer data from the IMAGE meridional magnetometer chain to determine the substorm phase at which the bipartite oval events occurred. The substorm event examined in this paper had a west-

ward electrojet centered near the northern end of the IMAGE chain and was just entering recovery phase as FAST passed overhead. For more information about the use of the IMAGE chain, see *Lühr et al.* [1998].

3. Observations

Plate 1 shows a series of LBHl images, obtained on June 6, 1997, between 1630 and 1745 UT. Geographic latitude and longitude lines are also shown. Plate 1a shows a bipartite structure for a previous substorm that occurred over Russia. It occurs on the dayside, prior to the FAST overflight, and it will not be discussed further in this paper. The bipartite structure discussed in this paper can first be seen in Plate 1b, at the right near the 0° meridian. By 1715 UT (see Plate 1d) this structure has developed into two separate and steady bands of UV emission. Note that this bipartite structure is present prior to, and persists after, the FAST overflight.

Plate 2 shows a series of LBHl images obtained during FAST overflight of the nightside bipartite structure. These images are mapped into magnetic local time and invariant latitude coordinates. It is important to note that the bipartite structure is relatively steady throughout this interval. A significant, star-derived correction to the assumed pointing direction of UVI was used to produce Plate 2. This correction resulted in an improved agreement of the electron energy fluxes estimated from UVI with those measured by FAST.

Figure 1 shows data from the IMAGE magnetometer chain. At roughly 1640 UT a substorm onset was observed. This onset was localized over northern Scandinavia (between the Hopen Island (HOP) and Kilpisjärvi (KIL) stations at 72.8° and 65.6° geomagnetic latitude, respectively). The recovery phase of this substorm began at roughly 1705 UT.

Plate 3 summarizes the FAST data during overflight of the bipartite oval. Plate 3a (Plate 3b) shows the energy flux of precipitating (upgoing) electrons within 30° of the local geomagnetic field line. Atmospheric photoelectrons, the band of significant flux below 70 eV, are visible throughout this event in the upgoing electrons, and the reflection of this population is seen throughout the poleward oval in the precipitating electrons. Plate 3c shows the total energy flux deposited into the ionosphere by precipitating electrons, assuming that no further acceleration occurs below the altitude of FAST. Also shown is the nominal UVI threshold level. After 1721 the electron energy flux from FAST dips below this level for ~30 s. This interval of weaker precipitation corresponds to the gap in UV emission which allows us to identify the bipartite oval. Plate 3d shows the anisotropy of the downgoing electrons, here defined as the ratio of flux near 0° to that near 45° pitch angle. The anisotropy is generally larger in the poleward oval than in the equatorward and is largest at the edges of strong precipitation regions. Plate 3e shows the component of the magnetic deviation (relative to IGRF95 plus secular variation) which is perpendicular to both the model field and the spacecraft velocity. The time derivative of this component is the usual proxy for field-aligned currents. Three probable current systems are indicated: (1) an

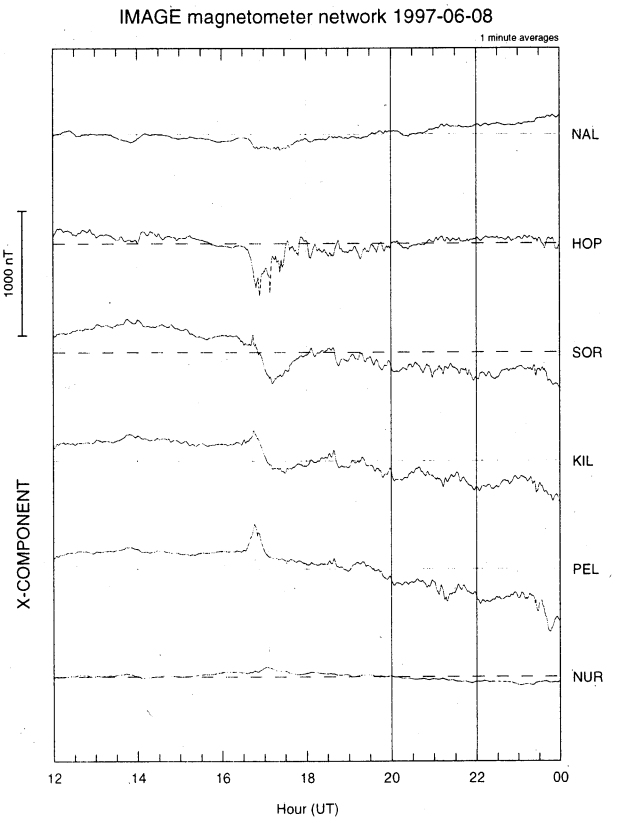

Figure 1. Plots of the magnetic northward component from selected IMAGE magnetometer stations. The stations lie between 57° and 76° north geomagnetic latitude and are arranged in order from north to south.

upward current from 1720 to 1721 UT, (2) a downward current from 1721 to 1722 UT, and (3) a downward current from 1724:30 to 1724:35. The interval 1722:30-1724:30 shows little or no field-aligned current. Plate 3g shows the energy flux of precipitating ions, again within 30° of the geomagnetic field. Several dispersive signatures, generally with energies that decrease with decreasing latitude, are visible from 1721 UT onward. Plate 3h shows the ion pitch angle distribution as a function of time. Note that the range of angular scale here is 0°-360°. For displayed angles <180°, this corresponds to the usual definition of pitch angle: the angle between the particle velocity and the geomagnetic field. For displayed angles >180° one must subtract the displayed value from 360° to obtain the pitch angle. Thus each pitch angle is sampled twice at each instant of time. This mode of display is a matter of convenience and is not intended to test for nongyrotropic distributions. (It can occasionally reveal instrumental or payload effects.) We see three types of ion pitch angle distribution: isotropic with loss cone (before 1724:30 UT, with the exception of 1720:30-1721:05 UT), isotropic (1720:30-1721:05 UT), and trapped (after 1724:30 UT). Note also that the color scale on Plates 3g and 3h is substantially enlarged from that of Plates 3a and 3b; thus the energy fluxes due to ions are two orders of magnitude smaller than those due to electrons, throughout this event. The final panel marks the intervals when UVI images are

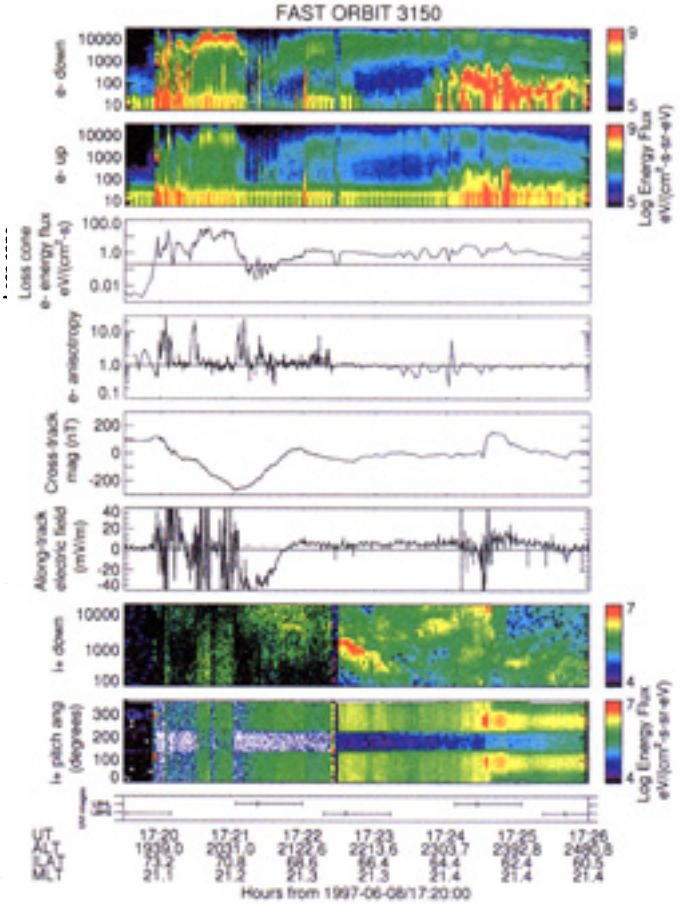

Plate 3. Data from the FAST overflight of the bipartite oval: (a) precipitating electrons, (b) Upgoing electrons, (c) precipitating electron energy flux, (d) electron anisotropy (ratio of precipitating flux to flux at 45° pitch angle), (e) magnetic perturbation, perpendicular to both IGRF95 and the spacecraft velocity, (f) electric field component, perpendicular to both IGRF95 and the spacecraft spin axis, (g) precipitating ions, and (h) pitch angle distribution of ions with energies from 0.1 to 30 keV. The bottom panel indicates the time intervals during which the UVI images were acquired.

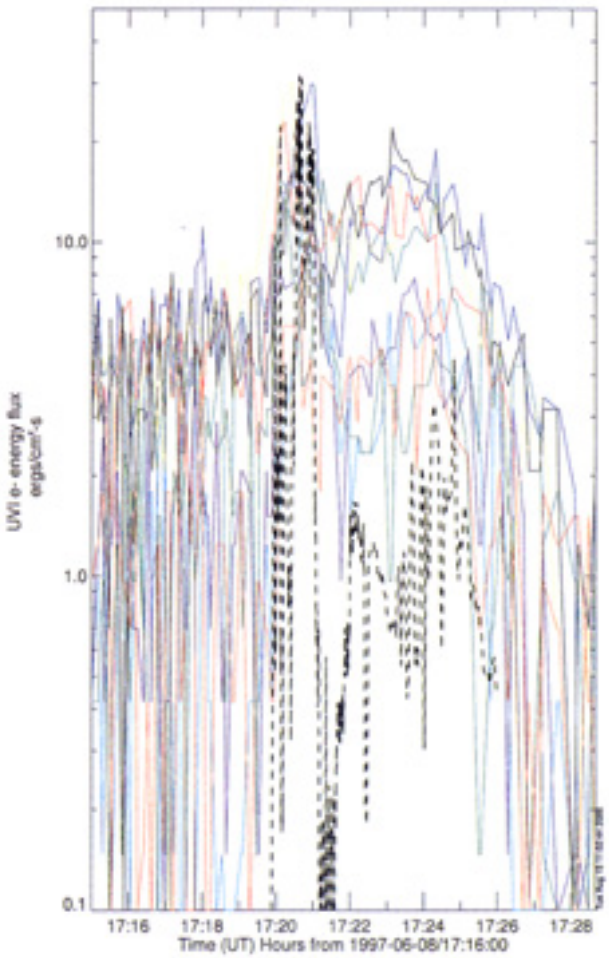

Plate 4. A direct comparison of FAST- and UVI-derived electron energy fluxes. The multiple superposed UVI profiles are taken, one from each image, from all locations crossed by the FAST track during the overflight. The thick dashed line is from FAST. From 1720-1721, in the poleward oval, the agreement is reasonable, but a significant discrepancy occurs in the equatorward oval.

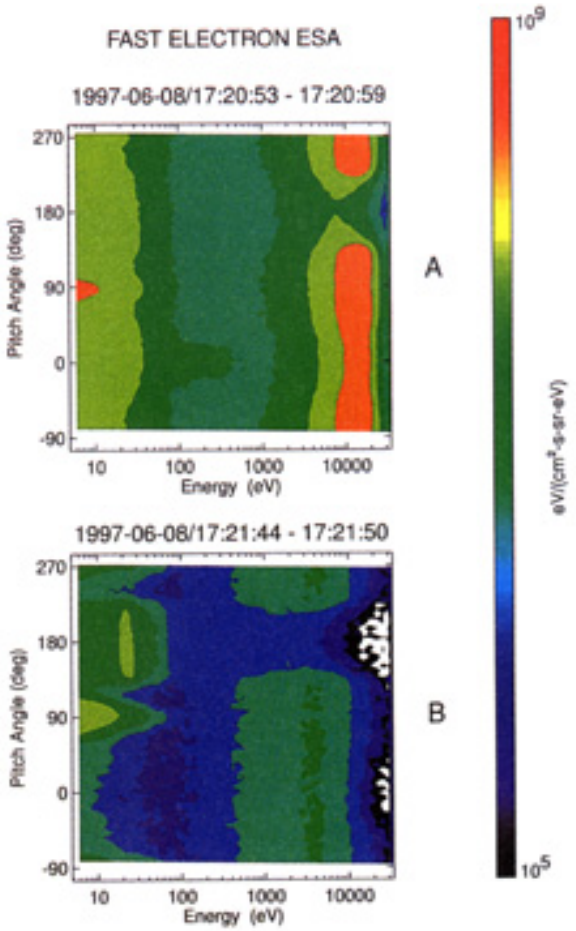

Plate 5. Representative electron energy flux versus pitch angle and energy plots for each of the two emission regions.

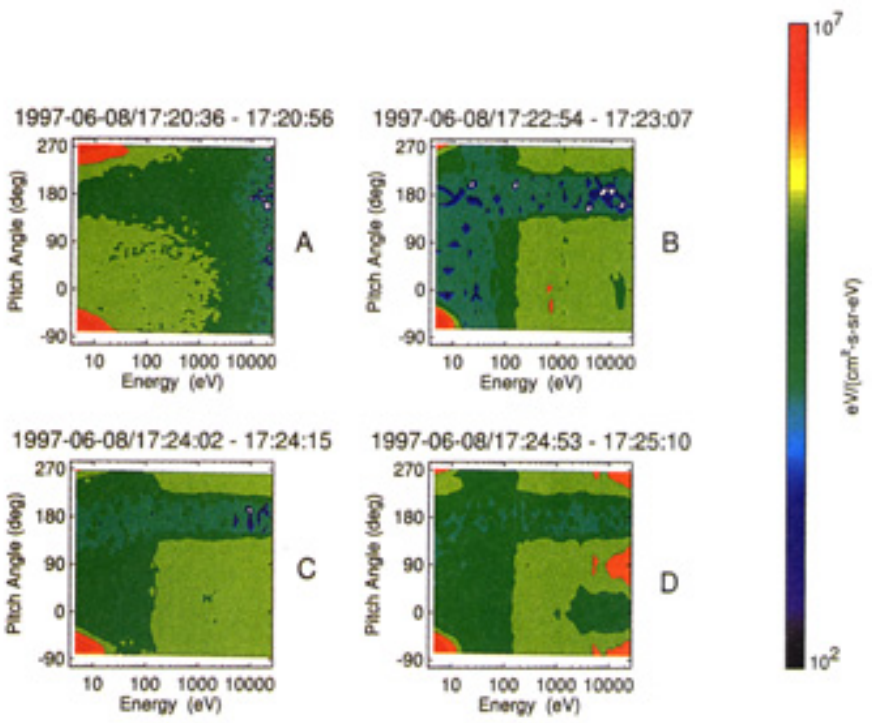

Plate 6. Representative ion energy flux versus pitch angle and energy plots from (a) the poleward oval, (b) the equatorward oval, (c) the poleward side of the "equatorward boundary current," and (d) the equatorward side of same.

being acquired; the duty cycle was roughly 50% during the FAST overflight.

Plate 4 shows a comparison between the precipitating electron energy flux inferred from auroral UV brightness and that measured directly by FAST. The UVI component of Plate 4 is produced by sampling, from all images taken during the FAST pass, the intensity in all the pixels visited by FAST. The locations of these intensities are then translated into times using the FAST orbit data. Of course, this procedure is sensible only during intervals where the auroral emission is relatively steady, as is the case here. Comparison between FAST and UVI is quite difficult to make owing to the drastically different scale lengths sampled by these two instruments as well as the precise pointing of UVI required. In this case the comparison was possible only because a known UV star was seen by UVI roughly 45 min prior to the FAST pass, and this star was used to correct the nominal UVI pointing for this event. The pointing correction, in this case, was $\sim 0.3°$. This is within the error bar of the nominal attitude specification of the Polar spacecraft and is equivalent to a shift of nearly 2 min on the time axis of Plate 4.

Plate 5a shows a typical electron energy flux distribution measured in the poleward oval, while Plate 5b is from the equatorward oval. (The angular scales here have the same meaning as that of Plate 3h; please see the explanatory note above). The enhancements seen at 90° pitch angle, at low energies, are from spacecraft photoelectrons. Comparing these two distributions, one can see that the equatorward energetic flux is less intense and, indeed, less energetic. Note also the absence of downgoing photoelectrons in the equatorward distribution.

Plates 6a-6d show typical examples of the four types of ion distributions seen during the overflight. The enhancements seen at -90° and at 270° are a spacecraft ram or sunlight contamination effect. Plate 6a shows the weak loss cone distribution seen throughout the poleward oval. Note, however, that there are some ions coming up in the loss cone during this time. Plate 6b shows the absence of low-energy ions in the equatorward oval: there is nothing at this time but the atmospheric loss cone. Plates 6c and 6d show the transition from single to double loss cone, which occurs at 1724:30 UT.

3.1. Electron Precipitation

The electron energy flux measured by FAST during this event (see Plate 3c) is separated, by a region of weak energy flux from 1721:05 to 1721:35 UT, into two intervals which clearly correspond to the two UV emission regions of the bipartite oval. The electron data (see Plates 3a and 3b) show that the two UV emission regions of the bipartite auroral oval are produced by two distinct types of electron precipitation. In the equatorward oval, from roughly 1721 until 1726 UT, Plate 3a shows that the precipitation is relatively broad in energy, with no sharp peak. The electron distribution function (see Plate 5) in this region consists of two main components. First, there is an extremely isotropic flux from 1 to 10 keV, with an atmospheric loss cone of roughly 30° half width. The isotropy of this precipitating component is consistent with the absence of significant parallel acceleration above FAST. Furthermore, this distribution can be modeled very well with an unaccelerated Maxwellian, with a temperature of 2 keV (calculation not shown). The second significant component of the equatorward oval electron distribution is the upgoing population which fills the loss cone at low (<60 eV) energies. These are atmospheric photoelectrons. Note that their angular distribution (loss cone filling) indicates that they originate from roughly the same altitude at which the precipitating electrons are lost to the atmosphere. Their presence at FAST is a clear indication that there is no significant difference in electric potential between FAST and the auroral emission altitude at this time.

In any region in which it can be shown that no further downward acceleration occurs below the altitude of FAST (e.g., this entire event), we expect that the total electron energy flux measured by FAST should compare well with that measured by UVI. In the poleward oval the comparison is, in fact, remarkably good. In the equatorward oval, however, UVI estimates a larger energy flux than FAST. This discrepancy, where UVI (FAST) appears to overestimate (underestimate) the electron energy flux in diffuse precipitation regions, is a generic feature of UVI-FAST comparisons, the significance of which will be discussed in a forthcoming paper.

In the poleward oval (before roughly 1722:30, see Plate 3d) the electron precipitation often has an anisotropy consistent with substantial low-altitude parallel acceleration. This anisotropy (the ratio of flux near 0° to that near 45° pitch angle) is largest when the energy of the "monoenergetic peak" is changing rapidly, e.g., just after 1720, near 1720:30, and just after 1721. Precipitation in the poleward oval is nearly always more field-aligned than that in the equatorward oval. The presence of highly field-aligned electron fluxes at the edges of auroral arcs has been observed previously and in this event may be due to the sort of suprathermal electron bursts described by *Johnstone and Winningham* [1982] and *Arnoldy et al.* [1974, 1985], or may be more closely related to the quasi-steady field-aligned precipitation observed near the edge of a quiet arc by *McFadden et al.* [1986].

The presence at FAST of upgoing atmospheric photoelectrons, throughout most of this event, is a clear indication that there is no further downward parallel acceleration occurring below the spacecraft; if there were, these low-energy upgoing electrons would be blocked by it. These electrons appear in Plate 3b as the red band below ~ 70 eV. (The 5 s modulation, visible in the photoelectrons throughout most of the pass, is due to spacecraft spin.) Parallel acceleration occurring above FAST would also be expected to reflect these photoelectrons so that they would appear in the downgoing channel, and indeed, this does occur throughout most of the poleward oval, but usually not in the equatorward oval, where it appears that (with the exception of the interval from 1722:00 to 1722:30) there is no downward acceleration at all.

The angular distribution of the downgoing atmospheric photoelectrons is of particular interest, since it constrains the physical process by which they are being returned earthward. We find that the angular distribution of downgoing photoelectrons, whenever they are present, is identical to that of the corresponding upgoing photoelectrons. This is consistent with their specular reflection from somewhere above FAST, with no detectable pitch angle scattering.

3.2. Ion Distributions

The energy flux delivered to the ionosphere from precipitating ions is roughly two orders of magnitude less than that due to electrons, throughout this event. In the equatorward oval we see ion energy spectra in which spectral peaks rise in energy as we move toward the poleward edge of the equatorward oval. This ion population is not beam-like, but rather has a loss cone distribution. This ion signature differs from the velocity-dispersed ion signature (VDIS) previously reported by other investigators [see, e.g., *Elphinstone et al.*, 1995b; *Bosqued et al.*, 1993] in its scale size, energy width, and location.

The intense current at 1724:35 corresponds to a dramatic change in the ion pitch angle distribution; poleward of the current, the ions have a typical loss cone distribution, while equatorward of it, the perpendicular fluxes are more intense and energetic (>4 keV) than the parallel. This can be referred to as a double loss cone distribution. Plates 6a-6d show the ion energy flux distributions in the poleward oval, in the equatorward oval, poleward of the equatorward oval boundary current, and equatorward of the equatorward oval boundary current, respectively.

In the poleward oval the ion distributions are relatively featureless. From 1720 to 1721, there is weak ion precipitation at a broad range of energies. After 1721, between the poleward oval and the equatorward oval, the precipitation is still fairly weak but begins to occur mostly above 1 keV. This high-energy precipitation intensifies dramatically after 1722:30.

3.3. Field-Aligned Currents, Maxwell Stresses, and the Convection Electric Field

At 1720 UT, FAST enters the poleward oval, encountering intense fluxes of downgoing electrons which carry an upward current. The measured energetic electrons can account for most (~85%, calculation not shown) of this current, as determined by comparison with the magnetometer data. At 1721 UT the intense fluxes disappear, and we see a downward current of similar intensity; the net current (in mA/m) across these two regions is zero. Within the poleward part of the oval, the current is somewhat variable but overall is definitely upward, as is usually thought to be true of discrete aurora. The poleward oval current has an average density of 0.8 $\mu A/m^2$ and is closed fully by the poleward boundary current of the equatorward oval, which has an average density of 0.6 $\mu A/m^2$.

Field-aligned currents within the equatorward oval are weak and of indeterminate direction. From 1722 to 1724:30 UT the currents are too small to measure, although there is still substantial precipitation and UV emission at these times at the footpoints of these flux tubes. At the equatorward edge of the equatorward oval, however, at 1724:30 UT, FAST abruptly encounters a downward current which is an order of magnitude more intense than the others on this pass. This intense current corresponds to a sudden change in the ion distribution toward an energetic trapped population and coincides with the equatorward boundary of significant UV emission. A precise calculation (not shown) allows us to determine that the measured electrons ($\geq$60 eV) are not the carriers of this current; in fact, their contribution is in the wrong direction. Thus this current would appear to be carried primarily by unmeasured thermal electrons.

Magnetic perturbations can also be viewed in terms of stress applied to the conductive ionosphere (the so-called "*B, v* paradigm"; see *Parker* [1996] and *Strangeway et al.* [2000]). One can visualize the ionospheric footpoints of flux tubes dragging behind the flow imposed by the magnetosphere; the magnetic perturbation $\delta\vec{\mathbf{B}}$ thus points in the opposite (same) direction as the mapped magnetospheric flow in the Northern (Southern) hemisphere. This picture does not replace, and is in no way inconsistent with, Ampère's law. Rather, the validity of this convenient visualization arises from the enormous increase in collisionality encountered in moving from the magnetosphere to the ionosphere along a flux tube [see *Strangeway and Raeder*, 2001].

The component of $\delta\vec{\mathbf{B}}$ displayed in Plate 3e is essentially westward; thus the magnetometer signal is indicating uniform eastward flow over the polar cap, followed by a strong shear toward westward high-altitude flow over the poleward oval. The high-altitude flow returns to zero in the gap between poleward oval and equatorward oval and remains relatively weak throughout the equatorward oval. Two abrupt shears (first eastward then westward), at the equatorward boundary of the equatorward oval, return the high-altitude flow to a relatively weak and neutral state.

Plate 3f shows the cross-track component of the electric field. Although this field reached values as large as $\pm$150 mV/m in the poleward oval, the plotting range was restricted to $\pm$40 mV/m; this was done to allow easy comparison with the relatively small corotation electric field, shown by the dashed green line. This is the value one would expect to see if the local plasma velocity was equal to the velocity of corotation, $\vec{\mathbf{v}}_{CR} = \vec{\omega} \times \vec{\mathbf{r}}$, where $\vec{\omega}$ is the angular velocity of the Earth and $\vec{\mathbf{r}}$ is the location of the spacecraft in an Earth-centered frame. When this electric field is greater (less) than the corotation value, the local plasma flow is eastward (westward). Note that in the poleward oval, before 1721:10, the low-altitude plasma flow (local to FAST) is not correlated, even in direction, with the high-altitude magnetospheric flow (as indicated by the magnetometer data). This is consistent with the presence of a parallel electric field above FAST; this same parallel field accelerates the auroral primaries and reflects the atmospheric photoelectrons.

Note the absence of reflected photoelectrons from 1721:20 to 1722:00, which indicates the lack of a parallel electric field on these flux tubes. Because there is no parallel field here, we expect the magnetospheric and ionospheric flows to

be strongly coupled, and indeed, the electric field and magnetic perturbation become correlated for this interval.

From 1722:00 to 17:22:40, there is once again a parallel field above FAST, indicated by the reflected atmospheric photoelectrons. During this time the electric field dwells near the corotation value, while $\delta\vec{\mathbf{B}}$ indicates a weakly shearing westward flow at high altitudes (above the decoupling parallel field). From 1722:40 until 1724:10 the magnetic perturbation is, within measuring uncertainty, zero. This is consistent with the apparent absence of applied stresses on these flux tubes; that is, the plasma is corotating throughout this interval, as is clearly seen in Plate 3f.

4. Summary

We have presented data from the overflight of one example of an auroral morphology which is commonly observed during the recovery phase of substorms. This morphology can be called the double, split, bifurcated, or bipartite oval. Our main point here is that the two similar bands of UV emission which form this morphology are, in fact, produced by two quite distinct physical processes.

The poleward oval is produced by electrons which undergo parallel acceleration at a relatively low-altitude (though still above FAST in the example we have presented). A significant field-aligned current is carried by these electrons. The high-altitude flow (indicated, at least in its direction, by magnetic perturbations local to FAST) appears to be decoupled from the low-altitude flow (as measured by the FAST electric field instrument). Such decoupling is consistent with the presence of a DC parallel field above FAST. Furthermore, the downgoing atmospheric photoelectrons, in the poleward oval, have a pitch angle distribution which is identical to that of the upgoing photoelectrons. In other words, they are specularly reflected, without detectable pitch angle scattering, consistent with a DC reflection process.

The equatorward oval, on the other hand, is produced by plasma sheet electrons, which appear to have undergone no parallel acceleration whatsoever. Furthermore, they do not carry a substantial field-aligned current. Throughout most of the equatorward oval, the atmospheric photoelectrons escape and are not reflected, which is, of course, consistent with the absence of parallel acceleration of the downgoing primaries. The absence of a parallel field leads one to expect a direct mapping of high-altitude (magnetospheric) flows to the ionosphere, and indeed, the magnetic perturbations and the electric field are consistent with this picture throughout most of the equatorward oval.

The events we have examined thus far (including the one presented in detail here), while interesting in terms of investigating the bipartite oval, are not at all extraordinary on the microscopic level, i.e., in the FAST data. Thus, while we have determined that the bipartite oval represents, in its two concentric pieces, two distinct microphysical situations, we are not able to determine what, if anything, is indicated macroscopically by the observation of a bipartite oval.

Acknowledgments. We thank the institutes who maintain the IMAGE magnetometer array. This work was supported by NASA grant NAG 5-7732.

Janet G. Luhmann thanks Patrick Newell and another referee for their assistance in evaluating this paper.

References

Arnoldy, R. L., P. B. Lewis, and P. O. Isaacson, Field-aligned auroral electron fluxes, *J. Geophys. Res., 79*, 4208-4221, 1974.

Arnoldy, R. L., T. E. Moore, and L. J. Cahill Jr., Low-altitude field-aligned electrons, *J. Geophys. Res., 90*, 8445-8460, 1985.

Bosqued, J. M., M. Ashour-Abdalla, M. El-Alaoui, L. M. Zelenyi, and A. Berthlier, AUREOL-3 observations of new boundaries in the auroral ion precipitation, *Geophys. Res. Lett., 20,* 1203-1206, 1993.

Carlson, C. W., R. F. Pfaff, and J. G. Watzin, The Fast Auroral SnapshoT (FAST) mission, *Geophys. Res. Lett., 25,* 2013-2016, 1998.

Elphinstone, R. D., et al., The double oval UV auroral distribution, 1, Implications for the mapping of auroral arcs, *J. Geophys. Res., 100*, 12,075-12,092, 1995a.

Elphinstone, R. D., et al., The double oval UV auroral distribution, 2, The most poleward arc system and the dynamics of the magnetotail, *J. Geophys. Res., 100*, 12,093-12,102, 1995b.

Johnstone, A. D., and J. D. Winningham, Satellite observations of suprathermal electron bursts, *J. Geophys. Res., 87*, 2321-2329, 1982.

Lühr, H., A. Aylward, S.C. Buchert, A. Pajunpää, K. Pajunpää, T. Holmboe, and S.M. Zalewski, Westward moving dynamic substorm features observed with the IMAGE magnetometer network and other ground-based instruments, *Ann. Geophys., 16*, 425-440, 1998.

Lummerzheim, D., M. Brittnacher, D. Evans, G. A. Germany, G. K. Parks, M. H. Rees, and J. F. Spann, High time resolution study of the hemispheric power carried by energetic electrons into the ionosphere during the May 19/20, 1996 auroral activity, *Geophys. Res. Lett., 24*, 987-990, 1997.

McFadden, J. P., C. W. Carlson, and M. H. Boehm, Field-aligned electron precipitation at the edge of an arc, *J. Geophys. Res., 91*, 1723-1730, 1986.

Parker, E. N., The alternative paradigm for magnetospheric physics, *J. Geophys. Res., 101*, 10,587-10,625, 1996.

Sanchez, E. R., B. H. Mauk, P. T. Newell, and C. I. Meng, Low-altitude observations of the evolution of substorm injection boundaries, *J. Geophys. Res., 98*, 5815-5838, 1993.

Strangeway, R. J., R. C. Elphic, W. J. Peria, and C. W. Carlson, FAST observations of electromagnetic stresses applied to the polar ionosphere, in *Magnetospheric Current Systems, Geophys. Monogr. Ser.,* vol. 118, edited by S. Ohtani et al., pp. 21-29, AGU, Washington, D. C., 2000.

Strangeway, R. J., and J. Raeder, On the transition from collisionless to collisional magnetohydrodynamics, *J. Geophys. Res., 106*, 1955-1960, 2001.

Torr, M. R., et al., A far ultraviolet imager for the International Solar-Terrestrial physics mission, *Space Sci. Rev., 71*, 329-383, 1995.

M. J. Brittnacher and W. J. Peria, Department of Earth and Space Sciences, University of Washington, Box 351310, Seattle, WA 98195, USA. (britt@geophys.washington.edu; peria@geophys.washington.edu)

C. W. Carlson and G. K. Parks, Space Sciences Laboratory, University of California, Berkeley, CA. 94720, USA. (cwc@ssl.berkeley.edu; parks@ssl.berkeley.edu)

(Received September 15, 2000; revised July 3, 2001; accepted July 3, 2001.)